



Cite this: *Nanoscale*, 2024, **16**, 9367

# Diffusioosmotic flow reversals due to ion–ion electrostatic correlations

Shengji Zhang <sup>a</sup> and Henry C. W. Chu <sup>\*b</sup>

Existing theories of diffusioosmosis have neglected ion–ion electrostatic correlations, which are important in concentrated electrolytes. Here, we develop a mathematical model to numerically compute the diffusioosmotic mobilities of binary symmetric electrolytes across low to high concentrations in a charged parallel-plate channel. We use the modified Poisson equation to model the ion–ion electrostatic correlations and the Bikerman model to account for the finite size of ions. We report two key findings. First, ion–ion electrostatic correlations can cause a unique reversal in the direction of diffusioosmosis. Such a reversal is not captured by existing theories, occurs at  $\approx 0.4$  M for a monovalent electrolyte, and at a much lower concentration of  $\approx 0.003$  M for a divalent electrolyte in a channel with the same surface charge. This highlights that diffusioosmosis of a concentrated electrolyte can be qualitatively different from that of a dilute electrolyte, not just in its magnitude but also its direction. Second, we predict a separate diffusioosmotic flow reversal, which is not due to electrostatic correlations but the competition between the underlying chemiosmosis and electroosmosis. This reversal can be achieved by varying the magnitude of the channel surface charge without changing its sign. However, electrostatic correlations can radically change how this flow reversal depends on the channel surface charge and ion diffusivity between a concentrated and a dilute electrolyte. The mathematical model developed here can be used to design diffusioosmosis of dilute and concentrated electrolytes, which is central to applications such as species mixing and separation, enhanced oil recovery, and reverse electrodialysis.

Received 1st December 2023,  
Accepted 3rd April 2024

DOI: 10.1039/d3nr06152c

rsc.li/nanoscale

## 1. Introduction

Diffusioosmosis refers to the deterministic fluid motion over a surface induced by a solute concentration gradient.<sup>1–7</sup> Diffusioosmosis comprises a chemiosmotic and an electroosmotic component. The chemiosmotic flow is generated by the osmotic pressure gradient induced by the solute gradient, which acts to drive fluid from a region of high to low solute concentration. The electroosmotic flow is generated by an electric field, which is induced by the ionic solute gradient to ensure no net ionic current in the bulk. The electroosmotic flow may drive fluid up or down the ionic solute gradient, depending on the diffusivities of ions and the charge of the surface. The diffusioosmotic flow velocity follows the ‘log-sensing’ relation,  $u = M \nabla \log n$ ,<sup>8</sup> where  $n$  is the ion concentration and a positive (negative) diffusioosmotic mobility  $M$  corresponds to fluid driven up (down) the solute gradient. Diffusioosmosis has received much attention in recent years

due to its impact on a wide range of applications, such as mixing and separation,<sup>9–36</sup> reverse electrodialysis,<sup>37–42</sup> and enhanced oil recovery.<sup>43–47</sup>

The main objective of this article is to demonstrate that ion–ion electrostatic correlations can lead to a unique reversal in the direction of diffusioosmosis of a binary, symmetric, concentrated electrolyte solution, relative to diffusioosmosis of the same but dilute electrolyte solution. Existing theories of diffusioosmosis have focused on dilute electrolyte solutions<sup>4,8,11,12,48–54</sup> and cannot capture this reversal. In a dilute electrolyte solution, the electric potential is typically modeled by the Poisson equation, where ions respond to the average potential in the electric double layer and the space charge density decays monotonically from the charged surface. The Poisson equation neglects electrostatic correlations between ions. Ion–ion electrostatic correlations are prominent in concentrated electrolytes and cause overscreening of charges on a surface, where the space charge density oscillates in sign near the charged surface.<sup>55–57</sup> By using molecular dynamics simulations and other non-local approaches,<sup>58–67</sup> it has been demonstrated that the causes of overscreening are ion–ion electrostatic correlations. Although these approaches can capture overscreening accurately, the high computational cost largely restricts their use to model equilibrium systems.

<sup>a</sup>Department of Chemical Engineering, University of Florida, Gainesville, FL 32611, USA<sup>b</sup>Department of Chemical Engineering and Department of Mechanical and Aerospace Engineering, University of Florida, Gainesville, FL 32611, USA.  
E-mail: h.chu@ufl.edu

Building on the work of Santangelo<sup>68</sup> and Hatlo and Lue,<sup>66</sup> Bazant *et al.*<sup>69,70</sup> derived a continuum-level, modified Poisson equation to robustly model overscreening. The equation is applicable to dilute and concentrated electrolyte solutions, room-temperature ionic liquids, and molten salts. For a binary electrolyte, the modified Poisson equation reads<sup>69–71</sup>

$$\varepsilon(l_c^2 \nabla^4 \phi - \nabla^2 \phi) = \rho = en_+ z_+ + en_- z_-, \quad (1)$$

where  $\varepsilon$  is the solution permittivity,  $\phi$  is the electric potential,  $\rho$  is the space charge density,  $e$  is the proton charge,  $n_+$  and  $n_-$  are the number densities of the cations and anions, respectively, and  $z_+$  and  $z_-$  are the valence of the cations and anions, respectively. For a symmetric electrolyte,  $z_+ = -z_- = z$ . The lower and upper bounds of the electrostatic correlation length,  $l_c$ , is set by two comparable length scales, namely, the hydrated ion diameter,  $a$ , and  $z^2 l_B$ , where  $l_B = e^2/(4\pi\epsilon kT)$  is the Bjerrum length with  $k$  the Boltzmann constant and  $T$  the absolute temperature. Because of its continuum nature, the modified Poisson equation can be coupled with other continuum-level transport equations and used to analyze dynamical problems efficiently. For instance, the modified Poisson equation can successfully capture non-equilibrium phenomena that follow from overscreening, including electroosmotic flow reversal,<sup>70</sup> electrophoretic mobility reversal,<sup>72</sup> dielectrophoretic polarization reversal,<sup>73</sup> and ionic current rectification reversal.<sup>74</sup>

In this article, we develop a mathematical model that predicts the diffusioosmotic mobilities of binary symmetric electrolytes across low to high concentrations in a channel comprising two charged parallel plates. We use the modified Poisson equation<sup>69</sup> to model the electric potential and electrostatic correlations. We incorporate the Bikerman model<sup>75</sup> to account for the finite size of ions. We report two key findings. First, we compute the diffusioosmotic mobilities of common electrolytes and demonstrate that the direction of diffusioos-

mosis of a monovalent electrolyte reverses as the electrolyte concentration increases beyond  $\approx 0.4$  M. This unique diffusioosmotic flow reversal is not captured by existing theories and we identify its origin to be overscreening of channel surface charges by ion-ion electrostatic correlations. In a channel with the same surface charge, we show that the diffusioosmotic flow reversal occurs at a much lower concentration of  $\approx 0.003$  M for a divalent electrolyte. Second, we present flow direction diagrams of diffusioosmosis as a function of the electrolyte concentration, valence, diffusivity, and channel surface charge. The diagrams predict a separate diffusioosmotic flow reversal to that shown in prior work.<sup>4,8,50,52</sup> This reversal is not due to electrostatic correlations but the competition between the chemiosmosis and electroosmosis that constitute diffusioosmosis. The reversal can be realized by varying the magnitude of the channel surface charge without changing its sign. However, due to electrostatic correlations, this reversal has a distinct dependence on the product of the channel surface charge and ion diffusivity between a concentrated and a dilute electrolyte.

The rest of this article is outlined as follows. In section 2, we formulate the problem by presenting the governing equations and boundary conditions for the electric potential, induced electric field, and diffusioosmotic flow field and mobility. In section 3, we present our results and elaborate on the two above-mentioned key findings. In section 4, we summarize this study and offer ideas for future work.

## 2. Problem formulation

Consider a channel that comprises two parallel plates of constant surface charge density  $q$  (or constant surface potential  $\zeta$ ) and a length  $L$  separated by a distance of  $2H$  (Fig. 1). A constant concentration gradient of a binary, symmetric electrolyte  $\nabla n_i^\infty$  is applied across the channel, where  $i = (+)$  and  $i = (-)$  are the cationic and anionic species, respectively, and  $n_+(x) = n_-(x) = n^\infty(x)$ . Following prior work,<sup>4,8,12,48–54</sup> we focus on typical regimes of diffusioosmosis, where the electrolyte concentration gradient across the channel length is much smaller than the background concentration,  $L|\nabla n^\infty|/n^\infty \ll 1$  with  $n^\infty = n^\infty(0)$ . A diffusioosmotic flow with a constant velocity  $\mathbf{u}$  is induced parallel to  $\nabla n_i^\infty$  along the  $x$ -direction. The velocity  $\mathbf{u}$

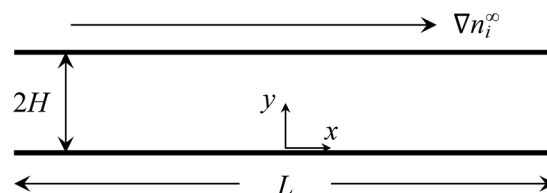
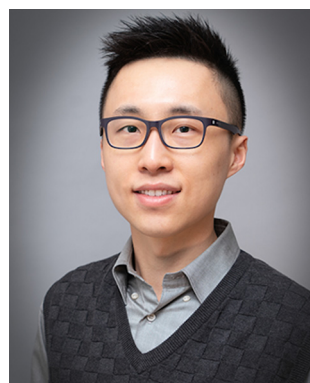


**Fig. 1** A constant concentration gradient of a binary, symmetric electrolyte  $\nabla n_i^\infty$  induces a diffusioosmotic flow in a channel that comprises two parallel plates of constant surface charge density and length  $L$  separated by distance  $2H$ . The diffusioosmotic flow is parallel to  $\nabla n_i^\infty$  along the  $x$ -direction.



**Henry C. W. Chu**

*Henry Chu is an Assistant Professor at the University of Florida (UF). He obtained an M. Phil. from The University of Hong Kong and a Ph.D. from Cornell University. He was a Postdoctoral Fellow at Carnegie Mellon University. His research group is developing predictive computational tools to address the National Academy of Engineering Grand Challenges in soft matter transport and design, collaborating with experimental*

*groups to translate knowledge into applications. His work has been recognized through awards, including the UF Global Faculty Fellowship, ACS PRF Doctoral New Investigator Grants, and U.S. DOE Geosciences Research Grants. He welcomes collaboration with academia, government agencies, and industry sponsors.*

is an unknown. In the following, we will determine the electric potential inside the channel in section 2.1 and the electric field induced by the electrolyte gradient in section 2.2. We will use this information to determine  $\mathbf{u}$  in section 2.3.

## 2.1. Electric potential

The Bikerman model<sup>75</sup> describes the electrochemical potential of each ionic species as  $\mu_{\pm} = kT \log n_{\pm} + z_{\pm} e \phi - kT \log[1 - a^3(n_{+} + n_{-})]$ , where the first two terms represent an ideal solution and the last term accounts for the steric effect of the finite size of ions. The steric effect is controlled by the bulk volume fraction of ions,  $\nu = 2a^3 n^{\infty}$ . At equilibrium,  $\nabla \mu_{\pm} = \mathbf{0}$ , the ion concentration follows the Fermi-like, modified Boltzmann distribution as<sup>14,52,76</sup>

$$n_{\pm} = a n^{\infty} e^{\frac{z_{\pm} e \phi}{kT}} \quad \text{with} \quad \alpha = \left[ 1 - \nu + \nu \cosh \left( \frac{ze\phi}{kT} \right) \right]^{-1}. \quad (2)$$

Substituting eqn (2) into (1) yields a Poisson–Fermi equation that governs the electric potential accounting for both the finite size of ions and ion–ion electrostatic correlations<sup>69,70</sup>

$$\varepsilon \left( l_c^2 \frac{d^4 \phi}{dy^4} - \frac{d^2 \phi}{dy^2} \right) = \rho = -2a n^{\infty} e z \sinh \left( \frac{ze\phi}{kT} \right). \quad (3)$$

We non-dimensionalize eqn (3) using the following schemes:  $\hat{y} = y/H$ ,  $\hat{\phi} = \phi/(kT/e)$ ,  $\hat{\kappa} = \kappa H$ , and  $\hat{\rho} = \rho/(n^{\infty} e z)$ , where quantities with carets are non-dimensional and the Debye length  $\kappa^{-1} \equiv \sqrt{\varepsilon kT/(2e^2 n^{\infty} z^2)}$  is the length scale over which the space charge density varies. The non-dimensionalized eqn (3) reads,

$$\delta_c^2 \frac{d^4 \hat{\phi}}{d\hat{y}^4} - \hat{\kappa}^2 \frac{d^2 \hat{\phi}}{d\hat{y}^2} = -\frac{\alpha \hat{\kappa}^4}{z} \sinh(z \hat{\phi}), \quad (4)$$

where  $\delta_c = \kappa l_c$  characterizes the importance of electrostatic correlations and is expected to be prominent when  $\delta_c \gtrsim O(1)$ .<sup>77</sup> Eqn (4) is subject to the following boundary conditions:<sup>69,70</sup>

$$\frac{d\hat{\phi}}{d\hat{y}} = -\hat{q} \quad \text{or} \quad \hat{\phi} = \hat{\zeta}, \quad \text{and} \quad \frac{d^3 \hat{\phi}}{d\hat{y}^3} = 0 \quad \text{at} \quad \hat{y} = 0, \quad (5)$$

$$\hat{\phi} = 0 \quad \text{and} \quad \frac{d\hat{\phi}}{d\hat{y}} = 0 \quad \text{at} \quad \hat{y} = 1. \quad (6)$$

In eqn (5), the first two conditions indicate that the channel surface charge density  $\hat{q} = qeH/(\varepsilon kT)$  or the channel surface potential  $\hat{\zeta} = \zeta e/(kT)$  is specified. The third condition is demanded by the Poisson–Fermi equation. In eqn (6), the conditions indicate that the electrostatic potential and its derivative approach zero smoothly away from the channel surface. The first condition is guaranteed, where our analyses focus on electrolyte solutions with  $n^{\infty} \geq 10^{-3} \text{ M}$  ( $\kappa^{-1} \lesssim 10^{-8} \text{ m}$ ) in typical microscale channels with  $H \gtrsim 10^{-7} \text{ m}$  so that  $\hat{\kappa} \geq 10$  and  $\hat{\phi} = 0$  at  $\hat{y} = 1$ . When  $\delta_c = 0$  ( $l_c = 0$ ) and  $\alpha = 1$  ( $\nu = 0$ ), eqn (4) reduces to the classical Poisson–Boltzmann equation for a dilute electrolyte solution, where the last condition in eqn (5) and (6) is not required.

## 2.2. Induced electric field

In diffusioosmosis, the electric field  $\mathbf{E}$  is generated by the imposed electrolyte concentration gradient to ensure no net ionic current in the bulk:<sup>8</sup>

$$\mathbf{J} = z_{+} e \mathbf{j}_{+} + z_{-} e \mathbf{j}_{-} = \mathbf{0}, \quad (7)$$

where the flux of individual species accounting for the finite size of ions is<sup>14,52,75</sup>

$$\mathbf{j}_i = -D_i \nabla n_i - \frac{D_i z_i e}{kT} n_i (\nabla \phi - \mathbf{E}) + n_i \mathbf{u} - \frac{\nu D_i n_i (\nabla n_{+} + \nabla n_{-})}{2n^{\infty} - \nu (\nabla n_{+} + \nabla n_{-})}, \quad (8)$$

with  $D_i$  the diffusivity of the  $i$ -th ionic species. Substituting eqn (8) into (7) gives

$$\mathbf{E} = E_x \mathbf{e}_x = \frac{kT |\nabla n^{\infty}|}{ze n^{\infty}} \left\{ \left[ \frac{(1+z\beta)e^{-z\hat{\phi}} - (1-z\beta)e^{z\hat{\phi}}}{(1+z\beta)e^{-z\hat{\phi}} + (1-z\beta)e^{z\hat{\phi}}} \right] \times \left( \frac{1}{1 - \alpha \nu \cosh(z\hat{\phi})} \right) + \frac{\text{Pe} \sinh(z\hat{\phi})}{(1+z\beta)e^{-z\hat{\phi}} + (1-z\beta)e^{z\hat{\phi}}} \hat{u} \right\} \mathbf{e}_x, \quad (9)$$

where  $\beta = (D_{+} - D_{-})/z(D_{+} + D_{-})$  is the ion diffusivity ratio,  $\mathbf{e}_x$  is the unit vector in the positive  $x$ -direction, the Peclet number  $\text{Pe} = 4n^{\infty} U/[(D_{+} + D_{-})|\nabla n^{\infty}|]$  describes the strength of the diffusioosmotic convection relative to ion diffusion,  $U = \varepsilon k^2 T^2 |\nabla n^{\infty}|/(\eta e^2 z^2 n^{\infty})$  is a characteristic velocity, and  $\hat{u} = u_x/U$  is the non-dimensionalized  $x$ -component of  $\mathbf{u}$ .

## 2.3. Diffusioosmotic flow field and mobility

Inertial forces are negligible in microscale transport. The fluid dynamics is described by the continuity equation,  $\nabla \cdot \mathbf{u} = \mathbf{0}$ , in addition to the Stokes equation with an electric body force,  $\mathbf{0} = \eta \nabla^2 \mathbf{u} - \nabla p + \rho(\mathbf{E} - \nabla \phi)$ . For a fully developed flow,  $u_x = u_x(y)$  and the continuity equation suggest that the  $y$ -component of  $\mathbf{u}$  is zero. Thus, the  $y$ - and  $x$ -components of the Stokes equation are written as

$$0 = -\frac{\partial p}{\partial y} - \rho \frac{d\phi}{dy}, \quad (10)$$

$$0 = \eta \frac{d^2 u_x}{dy^2} - \frac{\partial p}{\partial x} + \rho E_x, \quad (11)$$

where  $\eta$  is the dynamic viscosity of the electrolyte solution. The pressure  $p$  can be obtained by substituting eqn (2) into (10) and integrating with the boundary condition  $\hat{\phi} = 0$  at  $\hat{y} = 1$ ,

$$p = p^{\infty} - \frac{2kTn^{\infty}}{\nu} \log \alpha, \quad (12)$$

where  $p^{\infty}$  is a constant in the absence of an imposed pressure gradient. Finally, substituting eqn (12) into (11) gives the governing equation for the diffusioosmotic flow

$$0 = \frac{1}{\hat{\kappa}^2} \frac{d^2 \hat{u}}{d\hat{y}^2} - \frac{\log \alpha^{-1}}{\nu} + \frac{\hat{\rho} \hat{E}}{2}, \quad (13)$$

where  $-(\log \alpha^{-1})/\nu$  and  $\hat{\rho}\hat{E}/2$  are the chemiosmotic and electroosmotic driving forces to the diffusioosmotic flow, respectively, and  $\hat{E} = E_x/(kT|\nabla n^\infty|/zen^\infty)$ . Eqn (13) is subject to the no-slip condition at the channel walls and the symmetry condition about the channel centerline

$$\hat{u} = 0 \quad \text{at} \quad \hat{y} = 0, \quad \text{and} \quad \frac{d\hat{u}}{d\hat{y}} = 0 \quad \text{at} \quad \hat{y} = 1. \quad (14)$$

We further define the mean diffusioosmotic velocity as

$$\hat{u}_m \equiv \frac{u_m}{U} = \frac{\left(\int_0^H u_x dy\right)/H}{U} = \int_0^1 \hat{u} d\hat{y} = \hat{M}. \quad (15)$$

Note that  $\hat{u}_m$  is equivalent to the non-dimensionalized diffusioosmotic mobility  $\hat{M} = M\eta e^2 z^2 / (\epsilon k^2 T^2)$ , which together recover the dimensional log-sensing relation  $u_m = M \nabla \log n^\infty$ . In sum, we solved eqn (4)–(6) for  $\hat{\phi}$ . The potential  $\hat{\phi}$  is then used to compute  $\hat{\rho}$  via eqn (3) and is substituted into eqn (13) and (15) to solve for  $\hat{u}$  and  $\hat{u}_m$ . We use a combination of the finite difference method and Newton's method in Wolfram Mathematica to solve these equations and converged solutions are obtained with mesh size  $\Delta\hat{y} = 10^{-5}$ . Details of the numerical scheme are given in Appendix A. We validated our model by recovering the results of prior work<sup>50,52</sup> in Appendix B.

### 3. Results and discussion

In this section, we compute the non-dimensionalized diffusioosmotic mobilities  $\hat{M}$  of common binary, symmetric electrolytes. Their cation diffusivity, anion diffusivity, diffusivity ratio, and saturation concentration are listed in Table 1. In section 3.1, we present the mobilities as a function of the bulk molar concentration of the electrolyte  $C$ , which relates to the bulk number density of ions via  $n^\infty = 10^3 AC$ , where  $A$  is the Avogadro constant. In section 3.2, we present flow direction diagrams that show the direction of the diffusioosmotic flow as a function of the electrolyte concentration, valence, diffusivity, and channel surface charge. In section 3.1 and 3.2, we account for the fact that varying  $C$  varies  $\nu$ ,  $\hat{\kappa}$ , and  $\delta_c$ ; see section 2.1 for parameter definitions. We set  $T = 298$  K,  $a = 0.3$  nm,<sup>70,76</sup>  $l_c = z^2 l_B$ ,<sup>77</sup> and  $Pe = 4n^\infty U / [(D_+ + D_-) |\nabla n^\infty|] = 1$ , which is justified by typical diffusioosmosis with  $U \sim 10^{-6}$  ms<sup>-1</sup>,  $n^\infty / |\nabla n^\infty| \sim 10^{-3}$  m, and  $D_\pm \sim 10^{-9}$  m<sup>2</sup> s<sup>-1</sup>.<sup>10,50</sup>

#### 3.1. Variation of diffusioosmotic mobilities with bulk electrolyte concentrations

**3.1.1. Monovalent electrolytes ignoring electrostatic correlations ( $\delta_c = 0$ ).** First, we show and discuss the diffusioosmotic mobilities of monovalent electrolytes obtained by ignoring electrostatic correlations in Fig. 2. This will facilitate discussions in the next section on how electrostatic correlations can cause a unique diffusioosmotic flow reversal that is manifested in a sign reversal in the mobilities. As shown in Fig. 2(a), we compute the mobilities  $\hat{M}$  of five monovalent electrolytes: HCl ( $\beta = 0.64$ ), CH<sub>3</sub>COOK ( $\beta = 0.29$ ), KCl ( $\beta = -0.02$ ), NaCl ( $\beta = -0.21$ ), and NaOH ( $\beta = -0.60$ ). The channel height  $H = 100$  nm. Thus,  $\hat{\kappa} \approx 10$  at  $C = 10^{-3}$  M and  $\hat{\kappa} \geq 10$  as  $C$  increases. The channel surface charge density  $q = 0.014$  C m<sup>-2</sup> ( $\hat{q} = 78.4$ ) corresponds to a channel surface potential  $\zeta = 100$  mV ( $\hat{\zeta} = 4$ ) at  $C = 10^{-3}$  M. We use the same  $\hat{q}$  to compute the mobilities at other electrolyte concentrations. Fig. 2 includes the effect of finite-ion-size, i.e.,  $\nu$  is non-zero, but ignores electrostatic correlations by setting  $\delta_c = 0$ . By definition (Fig. 1), a positive (negative) mobility corresponds to a diffusioosmotic flow from a region of low (high) to high (low) electrolyte concentration.

The first observation from Fig. 2(a) is that, at a low electrolyte concentration  $C = 10^{-3}$  M for a strongly negative  $\beta = -0.60$  (grey line), the diffusioosmotic mobility is positive. That is, the diffusioosmotic flow is from a region of low to high electrolyte concentration. To understand this observation, we show the chemiosmotic driving force  $-(\log \alpha^{-1})/\nu$  in Fig. 2(b) and the electroosmotic driving force  $\hat{\rho}\hat{E}/2$  in Fig. 2(c) and (d) [see eqn (13)]; panel (d) is a zoom-in of panel (c). Fig. 2(b) shows that the chemiosmotic driving force is negative, meaning that a chemiosmotic flow is generated from a region of high to low electrolyte concentration, consistent with prior work.<sup>8</sup> The chemiosmotic driving force is independent of  $\beta$ , which explains the overlap of data for five different  $\beta$  values. Fig. 2(c) and (d) show that, for  $\beta = -0.60$ , the electroosmotic driving force is always positive away from the channel surface ( $\hat{y} = 0$ ), meaning that an electroosmotic flow is generated from a region of low to high electrolyte concentration. The positive electroosmotic driving force  $\hat{\rho}\hat{E}/2$  for  $\beta = -0.60$  is confirmed by its negative components  $\hat{\rho}$  and  $\hat{E}$  as shown in Fig. 2(e). To sum, since the magnitude of the electroosmotic driving force [Fig. 2(c)] is larger than the chemiosmotic driving force [Fig. 2(b)], the direction of the resulting diffusioosmotic flow is governed by

**Table 1** Cation diffusivity  $D_+$ , anion diffusivity  $D_-$ , diffusivity ratio  $\beta$ , and saturation concentration of common binary, symmetric electrolytes in water at temperature  $T = 298$  K<sup>78</sup>

Electrolyte	$D_+ [\times 10^{-9} \text{ m}^2 \text{ s}^{-1}]$	$D_- [\times 10^{-9} \text{ m}^2 \text{ s}^{-1}]$	$\beta$	Saturation concentration [M]
Hydrogen chloride (HCl)	9.31	2.03	0.64	19.7
Potassium acetate (CH <sub>3</sub> COOK)	1.96	1.09	0.29	27.4
Potassium chloride (KCl)	1.96	2.03	-0.02	4.61
Sodium chloride (NaCl)	1.33	2.03	-0.21	6.16
Sodium hydroxide (NaOH)	1.33	5.27	-0.60	25
Zinc sulphate (ZnSO <sub>4</sub> )	0.72	1.07	-0.10	3.57
Magnesium chromate (MgCrO <sub>4</sub> )	0.71	1.13	-0.12	5.15
Beryllium sulphate (BeSO <sub>4</sub> )	0.60	1.07	-0.14	3.81

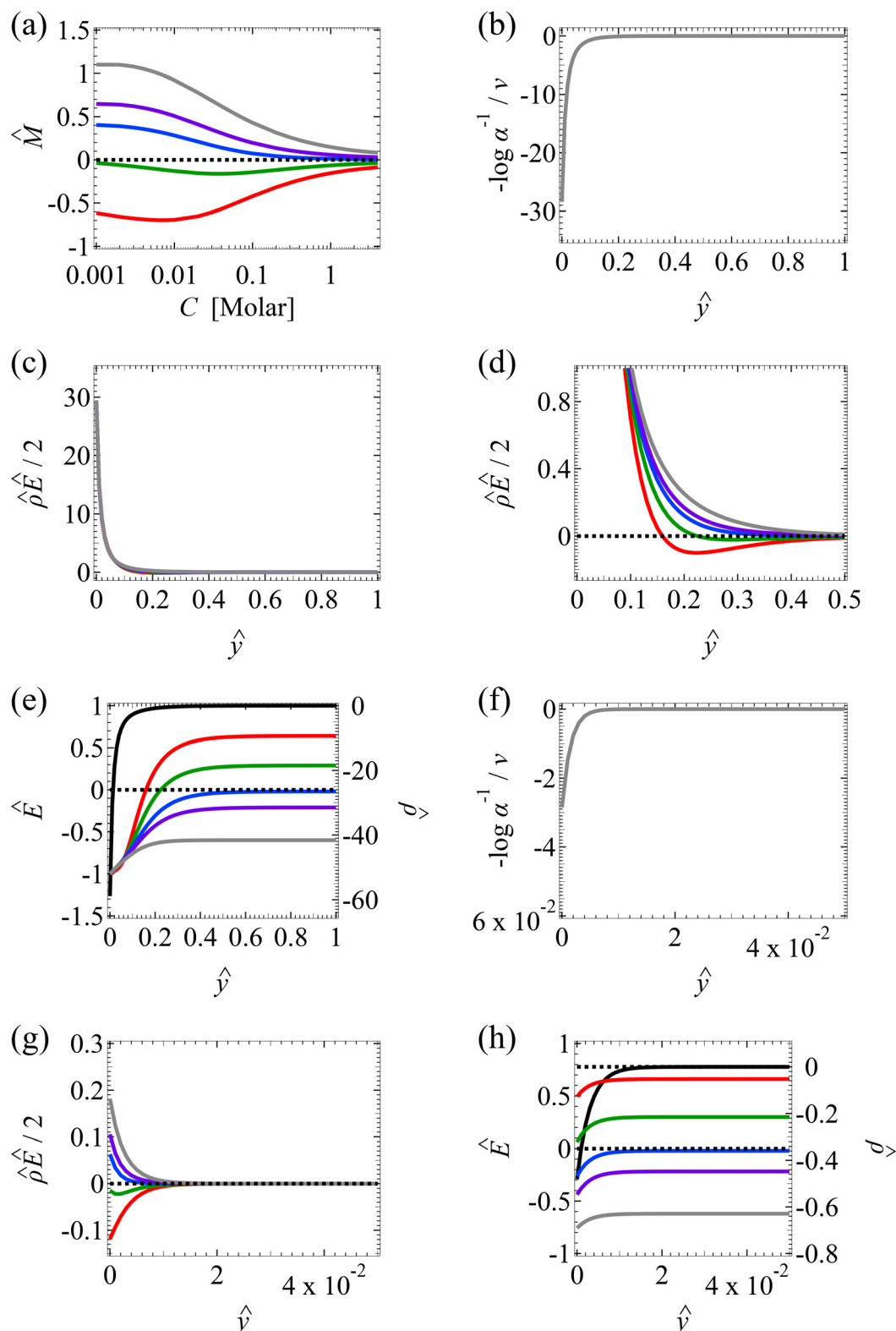


**Fig. 2** Diffusioosmosis of monovalent electrolytes ignoring electrostatic correlations ( $\delta_c = 0$ ). For panels (a)–(h), the red solid line denotes HCl (ion diffusivity ratio  $\beta = 0.64$ ), the green solid line denotes  $\text{CH}_3\text{COOK}$  ( $\beta = 0.29$ ), the blue solid line denotes KCl ( $\beta = -0.02$ ), the purple solid line denotes NaCl ( $\beta = -0.21$ ), the grey solid line denotes NaOH ( $\beta = -0.60$ ), and the dotted line is for referencing zero of the y-axis. The channel height  $H = 100$  nm and the channel surface charge density  $q = 0.014 \text{ C m}^{-2}$ . Panels (b)–(e) and (f)–(h) are computed at a bulk electrolyte molar concentration  $C = 10^{-3} \text{ M}$  and  $C = 1 \text{ M}$ , respectively. (a): The diffusioosmotic mobility  $\hat{M}$  versus  $\hat{y}$ . (b) and (f): The chemiosmotic driving force  $-\log \alpha^{-1}/\nu$  versus the distance from the bottom channel wall  $\hat{y}$ . (c) and (g): The electroosmotic driving force  $\hat{p}\hat{E}/2$  versus  $\hat{y}$ . (d): A zoom-in of panel (c) for showing a sign change of  $\hat{p}\hat{E}/2$ . (e) and (h): The space charge density  $\hat{p}$  (right y-axis; black solid line) and electric field  $\hat{E}$  (left y-axis; all other lines) versus  $\hat{y}$ .



the former, which goes from a region of low to high electrolyte concentration, *i.e.*, a positive mobility.

The second observation from Fig. 2(a) is that, at a low electrolyte concentration  $C = 10^{-3}$  M for a strongly positive  $\beta = 0.64$  (red line), the diffusioosmotic mobility is negative. That is, the diffusioosmotic flow is from a region of high to low electrolyte concentration. This can be understood by the same reasoning as in the above paragraph. Specifically, Fig. 2(b) shows that the chemiosmotic driving force  $-(\log \alpha^{-1})/\nu$  is negative, meaning that a chemiosmotic flow is generated from a region of high to low electrolyte concentration. Fig. 2(c) and (d) show that, for  $\beta = 0.64$ , the electroosmotic driving force  $\hat{\rho}\hat{E}/2$  is positive near the channel wall ( $y \lesssim 0.16$ ) and becomes negative away from the channel wall ( $y \gtrsim 0.16$ ). Such a change in the direction of the electroosmotic driving force is caused by a sign change in the induced electric field  $\hat{E}$  but not in the space charge density  $\hat{\rho}$  [Fig. 2(e)]. Thus, the net electroosmotic flow for  $\beta = 0.64$  is weaker than that for  $\beta = -0.60$ . Consequently, when the electroosmotic flow couples with the chemiosmotic flow for  $\beta = 0.64$ , the resulting diffusioosmotic flow is governed by the latter, which goes from a region of high to low electrolyte concentration, *i.e.*, a negative mobility.

Combining the first and second observations, at a low electrolyte concentration, the mobility transitions from positive to increasingly negative as  $\beta$  becomes more positive.

The third observation from Fig. 2(a) is that the magnitude of the mobility decreases and approaches zero with an increasing electrolyte concentration  $C$ . This can be understood by recalling that we consider a constant channel surface charge density  $\hat{q} = 78.4$ . This corresponds to a channel surface potential  $\hat{\zeta} = 4$  at a low electrolyte concentration  $C = 10^{-3}$  M. On increasing the electrolyte concentration, the channel surface potential decreases and approaches zero, *e.g.*,  $\hat{\zeta} = 0.24$  at  $C = 1$  M which can be obtained by solving eqn (4)–(6), and so does the mobility.

**3.1.2. Monovalent electrolytes accounting for electrostatic correlations ( $\delta_c = \kappa l_c$ ).** In this section, we demonstrate a unique diffusioosmotic flow reversal caused by electrostatic correlations. This reversal manifests in a sign reversal in the diffusioosmotic mobility at a high electrolyte concentration  $C \gtrsim 0.1$  M. To this end, we show Fig. 3 is obtained with the same parameters as Fig. 2, except that a non-zero  $\delta_c$  is input into the computation according to its definition ( $\delta_c = \kappa l_c$ ) instead of assuming it to be zero.

We start by stating the similarities between Fig. 3(a) and 2(a). These similarities occur when  $C < 0.1$  M, where the effect of electrostatic correlations is weak. First, Fig. 3(a) shows that, at a low electrolyte concentration  $C = 10^{-3}$  M, the mobility is negative for a strongly positive  $\beta$  (grey line) and transitions to be negative for a strongly positive  $\beta$  (red line). This trend and the physical explanations are identical to those presented in Fig. 2(a) at a low electrolyte concentration (the first and the second observation in section 3.1.1). In fact, the mobilities at  $C = 10^{-3}$  M in Fig. 3(a) and their constitutive driving forces in Fig. 3(b)–(e) are almost identical to

those in Fig. 2(a)–(e). This is because, at  $C = 10^{-3}$  M,  $\delta_c = 0.074 \ll 1$  in Fig. 3(a)–(e) indicates that electrostatic correlations are negligible and can be approximated accurately by neglecting electrostatic correlations ( $\delta_c = 0$ ) as presented in Fig. 2(a)–(e). Second, the same as in Fig. 2(a), Fig. 3(a) shows that the magnitude of the mobility decreases with an increasing electrolyte concentration. This echoes the third observation in section 3.1.1.

Next, let us state and discuss the new phenomena caused by electrostatic correlations, as shown by the dissimilarities between Fig. 3(a) and 2(a). These dissimilarities occur when  $C \gtrsim 0.1$  M, where the effect of electrostatic correlations is prominent. The first new phenomenon caused by electrostatic correlations is that, for a fixed  $\beta$  value, there is a substantial deviation of the mobility as shown in Fig. 3(a) relative to Fig. 2(a) at  $C \gtrsim 0.2$  M where  $\delta_c \gtrsim 1$ . This is consistent with the Poisson–Fermi eqn (4) in that the effect of electrostatic correlations is important when  $\delta_c \gtrsim O(1)$ .<sup>77</sup>

The second new phenomenon caused by electrostatic correlations is that the aforementioned deviation of the mobility in Fig. 3(a) subsequently evolves into a unique sign reversal in the mobility at  $C \gtrsim 0.4$  M, which is absent in Fig. 2(a). For instance, in Fig. 3(a) for  $\beta = -0.60$  (grey line) the mobility is positive at  $C = 10^{-3}$  M and becomes negative at  $C \gtrsim 0.4$  M, whereas in Fig. 2(a) for  $\beta = -0.60$  the mobility is positive at all concentrations  $C$ . A comparison between Fig. 3(f)–(h) (which accounts for electrostatic correlations) and Fig. 2(f)–(h) (which ignores electrostatic correlations) shows that electrostatic correlations are at the origin of such a sign reversal in the mobility at a high electrolyte concentration. First, by comparing Fig. 3(f) and 2(f), the chemiosmotic driving force  $-(\log \alpha^{-1})/\nu$  in the two panels are found to be qualitatively the same, indicating that the chemiosmotic flow is not a cause of the diffusioosmotic mobility reversal at a high electrolyte concentration. Second, by comparing Fig. 3(g) and 2(g), the electroosmotic driving force  $\hat{\rho}\hat{E}/2$  presented in Fig. 3(g) shows a sign reversal near  $y = 0.01$ , which is absent in Fig. 2(g). This indicates that the electroosmotic flow reversal away from the channel surface is the cause of the diffusioosmotic mobility reversal at a high electrolyte concentration. We remark that such a sign reversal in  $\hat{\rho}\hat{E}/2$  is due to the electrostatic correlation-induced overscreening of the channel surface charge, which is manifested in a sign change in the space charge density  $\hat{\rho}$  near the channel surface as shown in Fig. 3(h). This sign change in  $\hat{\rho}$  is absent when electrostatic correlations are ignored in Fig. 2(h). This sign change in  $\hat{\rho}$  has been reported in prior work and causes various anomalous electrokinetic phenomena, including electroosmotic flow reversal,<sup>70</sup> electrophoretic mobility reversal,<sup>72</sup> dielectrophoretic polarization reversal,<sup>73</sup> and ionic current rectification reversal.<sup>74</sup> In sum, electrostatic correlations cause overscreening of the channel surface charge that leads to a sign change in the space charge density near the channel surface. Such a sign change in the space charge density in turn causes a reversal in the electroosmotic driving force  $\hat{\rho}\hat{E}/2$  that generates the electroosmotic flow, leading to a sign reversal in the diffusioosmotic mobility.

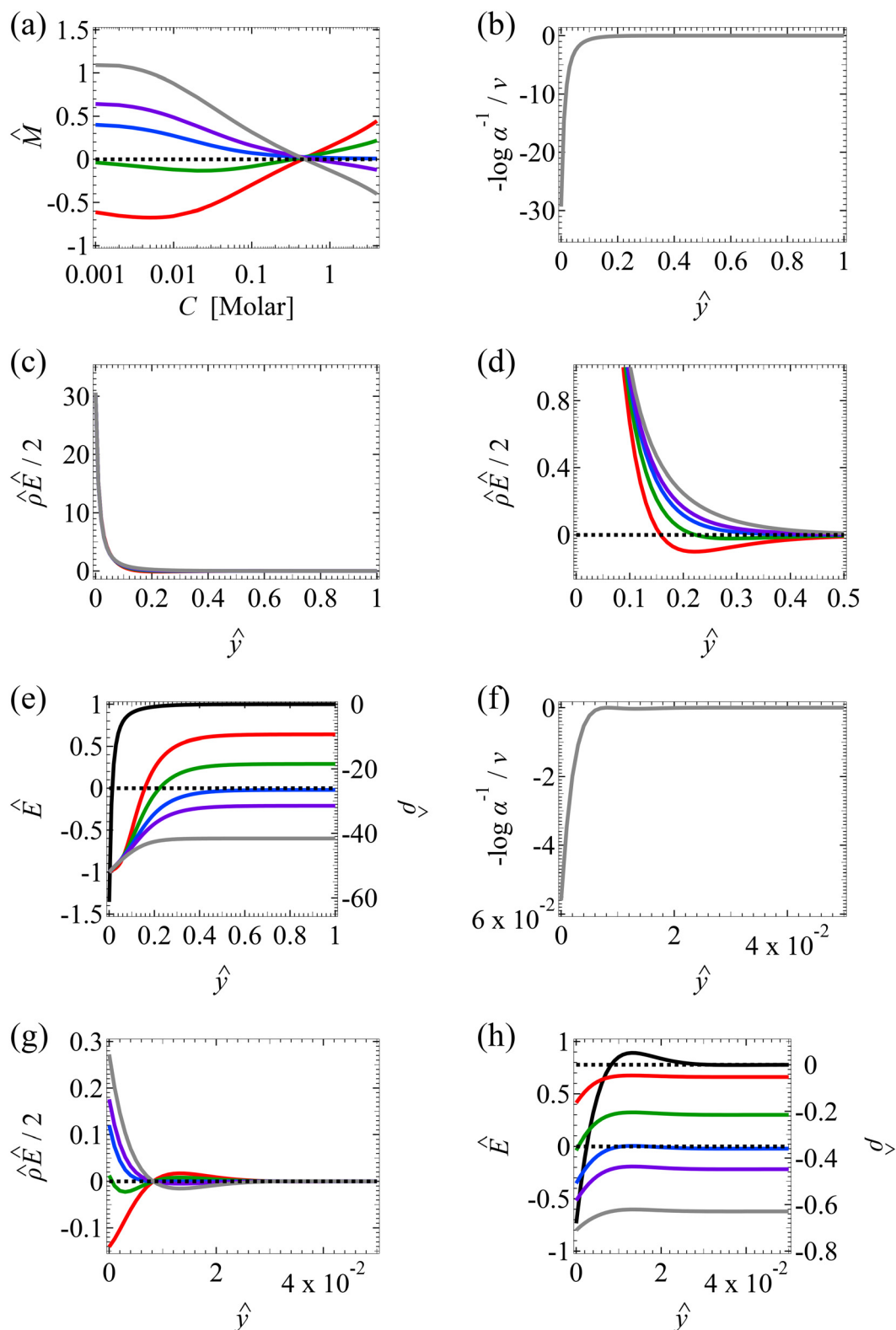


**Fig. 3** Diffusioosmosis of monovalent electrolytes accounting for electrostatic correlations ( $\delta_c = \kappa l_c$ ). Figure captions are the same as those in Fig. 2, except that electrostatic correlations are accounted for.

A further note to the above-mentioned second new phenomenon is that the unique sign reversal in the mobility is absent for  $\beta = -0.02$  (blue line) in Fig. 3(a), despite accounting

for electrostatic correlations. This is because for  $\beta = -0.02$  a sign change in  $\hat{E}$  and in  $\hat{\rho}$  [Fig. 3(h)] cancel each other, leading to no sign change in  $\hat{\rho}\hat{E}/2$  [Fig. 3(g)] and the electroosmotic

flow. Thus, without a sign change in the electroosmotic flow, there is no sign change in the diffusioosmotic mobility.

The third new phenomenon caused by electrostatic correlations is that, after the unique sign reversal in the mobility at  $C \gtrsim 0.4$  M, the mobility continues to increase in magnitude as shown in Fig. 3(a). The two physical underpinnings of this new phenomenon are as follows. First, in the presence of electrostatic correlations, the magnitude of the electroosmotic driving force  $\hat{\rho}\hat{E}/2$  [Fig. 3(g)] is larger than that when electrostatic correlations are neglected [Fig. 2(g)]. Second, overscreening as described by the Poisson–Fermi equation causes a non-vanishing and increasing channel surface potential at an electrolyte concentration of  $C \gtrsim 0.4$  M. Physically, the charge on the channel surface is overcompensated by a layer of counterions,<sup>69,72</sup> resulting in an increasing surface potential as the electrolyte concentration increases and electrostatic correlations become increasingly important. This is in contrast to the classical Poisson equation, which overlooks overscreening and predicts a vanishing channel surface potential at a high electrolyte concentration. For instance, at  $C = 1$  M, in Fig. 3(a) the channel surface potential  $\hat{\zeta} = 0.32$  whereas in Fig. 2(a) the channel surface potential  $\hat{\zeta} = 0.24$ . In sum, under electrostatic correlations, with a larger  $\hat{\rho}\hat{E}/2$  value and an increasing  $\hat{\zeta}$  value at a high electrolyte concentration, the diffusioosmotic mobility continues to increase in magnitude after the unique sign reversal.

**3.1.3. Divalent electrolytes ignoring electrostatic correlations ( $\delta_c = 0$ ).** We show the diffusioosmotic mobilities of divalent electrolytes obtained by ignoring electrostatic correlations in Fig. 4. In Fig. 4(a), we compute the diffusioosmotic mobilities of three divalent electrolytes:  $\text{ZnSO}_4$  ( $\beta = -0.10$ ),  $\text{MgCrO}_4$  ( $\beta = -0.12$ ), and  $\text{BeSO}_4$  ( $\beta = -0.14$ ). The channel height  $H = 100$  nm. Thus,  $\hat{\kappa} \approx 20$  at  $C = 10^{-3}$  M and  $\hat{\kappa} \geq 20$  as  $C$  increases. The channel surface charge density  $q = 0.014$  C m<sup>-2</sup> ( $\hat{q} = 78.4$ ) corresponds to a channel surface potential  $\zeta = 50$  mV ( $\hat{\zeta} = 2$ ) at  $C = 10^{-3}$  M. We use the same  $\hat{q}$  to compute the mobility at other electrolyte concentrations. Fig. 4 includes the effect of finite-ion-size, *i.e.*,  $\nu$  is non-zero, but ignores electrostatic correlations by setting  $\delta_c = 0$ . A positive (negative) mobility corresponds to a diffusioosmotic flow from a region of low (high) to high (low) electrolyte concentration. The observations from Fig. 4 and explanations largely follow those from Fig. 2 for monovalent electrolytes. We have summarized them below.

First, Fig. 4(a) shows that, at a low electrolyte concentration  $C = 10^{-3}$  M, the mobility transitions from a large positive number to a small positive number as  $\beta$  is increasingly positive. This trend and the physical explanations are identical to that in Fig. 2(a) at a low electrolyte concentration (the first and the second observation in section 3.1.1). Specifically, in Fig. 4(a) at  $C = 10^{-3}$  M, the positive mobility for  $\beta = -0.14$  (grey line) arises from the electroosmotic flow [Fig. 4(c)–(e)] dominating the chemiosmotic flow [Fig. 4(b)], where the former flows from a region of low to high electrolyte concentration, *i.e.*, a positive mobility. The smaller positive mobility for  $\beta = -0.10$  (red line) is due to the fact that the electroosmotic flow is weaker than that for  $\beta = -0.14$  [Fig. 4(c)–(e)], despite that it still dominates the chemiosmotic flow [Fig. 4(b)].

Second, Fig. 4(a) shows that the mobility decreases in magnitude with an increasing electrolyte concentration. This trend is identical to the third observation in section 3.1.1. The physical explanations are the same and not repeated here for brevity.

**3.1.4. Divalent electrolytes accounting for electrostatic correlations ( $\delta_c = \kappa l_c$ ).** In this section, we demonstrate that electrostatic correlations cause a unique sign reversal in the diffusioosmotic mobility of divalent electrolytes, similar to that shown in section 3.1.2 for monovalent electrolytes. To this end, we show Fig. 5 obtained with the same parameters as Fig. 4, except that a non-zero  $\delta_c$  is input into the computation according to its definition ( $\delta_c = \kappa l_c$ ) instead of assuming it to be zero. In the following, we state and discuss the new phenomena caused by electrostatic correlations, as shown by the dissimilarities between Fig. 5(a) and 4(a).

The first new phenomenon caused by electrostatic correlations is that, for a fixed  $\beta$ , there is a substantial deviation of the mobility in Fig. 5(a) compared to that in Fig. 4(a). This observation is similar to the first new phenomenon in section 3.1.2 for monovalent electrolytes. Specifically, this deviation is observed in monovalent electrolytes at  $C \geq 0.2$  M by comparing Fig. 3(a) and 2(a). However, this deviation occurs at a lower electrolyte concentration  $C \geq 10^{-3}$  M for divalent electrolytes as observed by comparing Fig. 5(a) and 4(a). This can be understood as follows. First, the inverse Debye length of a divalent electrolyte is twice that of a monovalent electrolyte,  $\kappa_{\text{di}} = 2\kappa_{\text{mono}}$ . Second, the electrostatic correlation length of a divalent electrolyte is four times that of a monovalent electrolyte,  $l_{c,\text{di}} = 4l_{c,\text{mono}}$ . Combining these two statements, it is computed that, at  $C = 10^{-3}$  M,  $\delta_c (= \kappa l_c) = 0.59$  for a divalent electrolyte whereas  $\delta_c = 0.074$  for a monovalent electrolyte. That is, at  $C = 10^{-3}$  M, the effect of electrostatic correlations is prominent in divalent electrolytes but not in monovalent electrolytes. Hence, consistent with the Poisson–Fermi equation that the impact of electrostatic correlations increases with  $\delta_c$ , at the same concentration the deviation of the mobility in divalent electrolytes [comparing Fig. 5(a) and 4(a)] is more prominent than that in monovalent electrolytes [comparing Fig. 3(a) and 2(a)].

The second new phenomenon caused by electrostatic correlations is that there is a unique sign reversal in the mobility at  $C \approx 0.003$  M in Fig. 5(a), which is absent in Fig. 4(a). A comparison between Fig. 5(f)–(h) (which accounts for electrostatic correlations) and Fig. 4(f)–(h) (which ignores electrostatic correlations) shows that electrostatic correlations are at the origin of such a sign reversal. The phenomenon and physical explanations here are identical to those in the discussion of the second new phenomenon in section 3.1.2 and are reiterated briefly as follows. Electrostatic correlations result in overscreening of the channel surface charge and a sign change in the space charge density near the channel surface [Fig. 5(h)]. Such a sign change in the space charge density in turn induces a reversal in the electroosmotic driving force  $\hat{\rho}\hat{E}/2$  and electroosmotic flow [Fig. 5(g)], leading to a sign reversal in the diffusioosmotic mobility [Fig. 5(a)]. We note that such a mobility reversal due to electrostatic correlations occurs at a lower con-



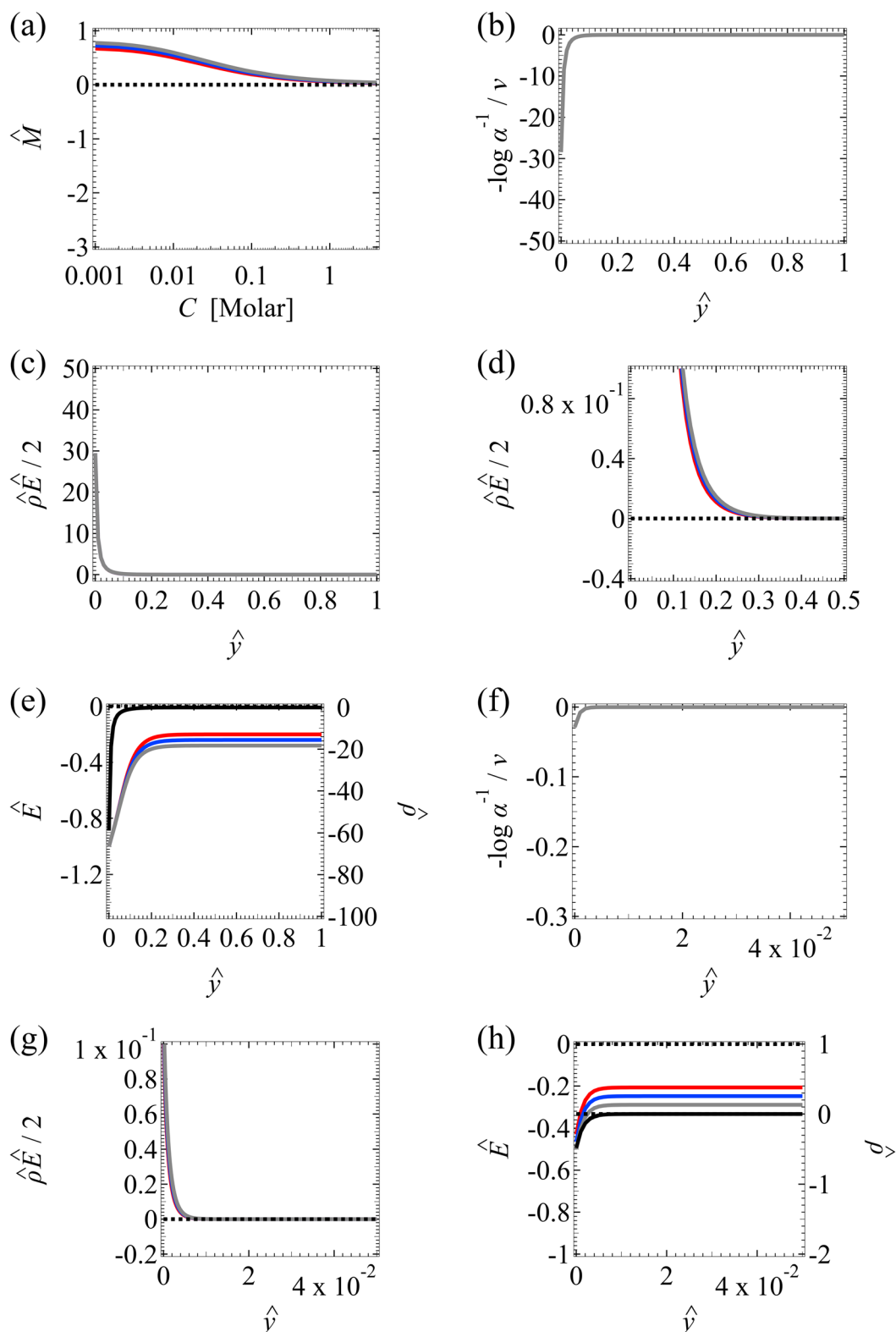


**Fig. 4** Diffusioosmosis of divalent electrolytes ignoring electrostatic correlations ( $\delta_c = 0$ ). For panels (a)–(h), the red solid line denotes  $\text{ZnSO}_4$  (ion diffusivity ratio  $\beta = -0.10$ ), the blue solid line denotes  $\text{MgCrO}_4$  ( $\beta = -0.12$ ), the grey solid line denotes  $\text{BeSO}_4$  ( $\beta = -0.14$ ), and the dotted line is for referencing zero of the  $y$ -axis. The channel height  $H = 100$  nm and channel surface charge density  $q = 0.014 \text{ C m}^{-2}$ . Panels (b)–(e) and (f)–(h) are computed at a bulk electrolyte molar concentration  $C = 10^{-5} \text{ M}$  and  $C = 1 \text{ M}$ , respectively. (a): The diffusioosmotic mobility  $\hat{M}$  versus  $\hat{y}$ . (b) and (f): The chemiosmotic driving force  $-\log \alpha^{-1}/\nu$  versus the distance from the bottom channel wall  $\hat{y}$ . (c) and (g): The electroosmotic driving force  $\hat{\rho}\hat{E}/2$  versus  $\hat{y}$ . (d): A zoom-in of panel (c) for showing a sign change of  $\hat{\rho}\hat{E}/2$ . (e) and (h): The space charge density  $\hat{\rho}$  (right  $y$ -axis; black solid line) and electric field  $\hat{E}$  (left  $y$ -axis; all other lines) versus  $\hat{y}$ .

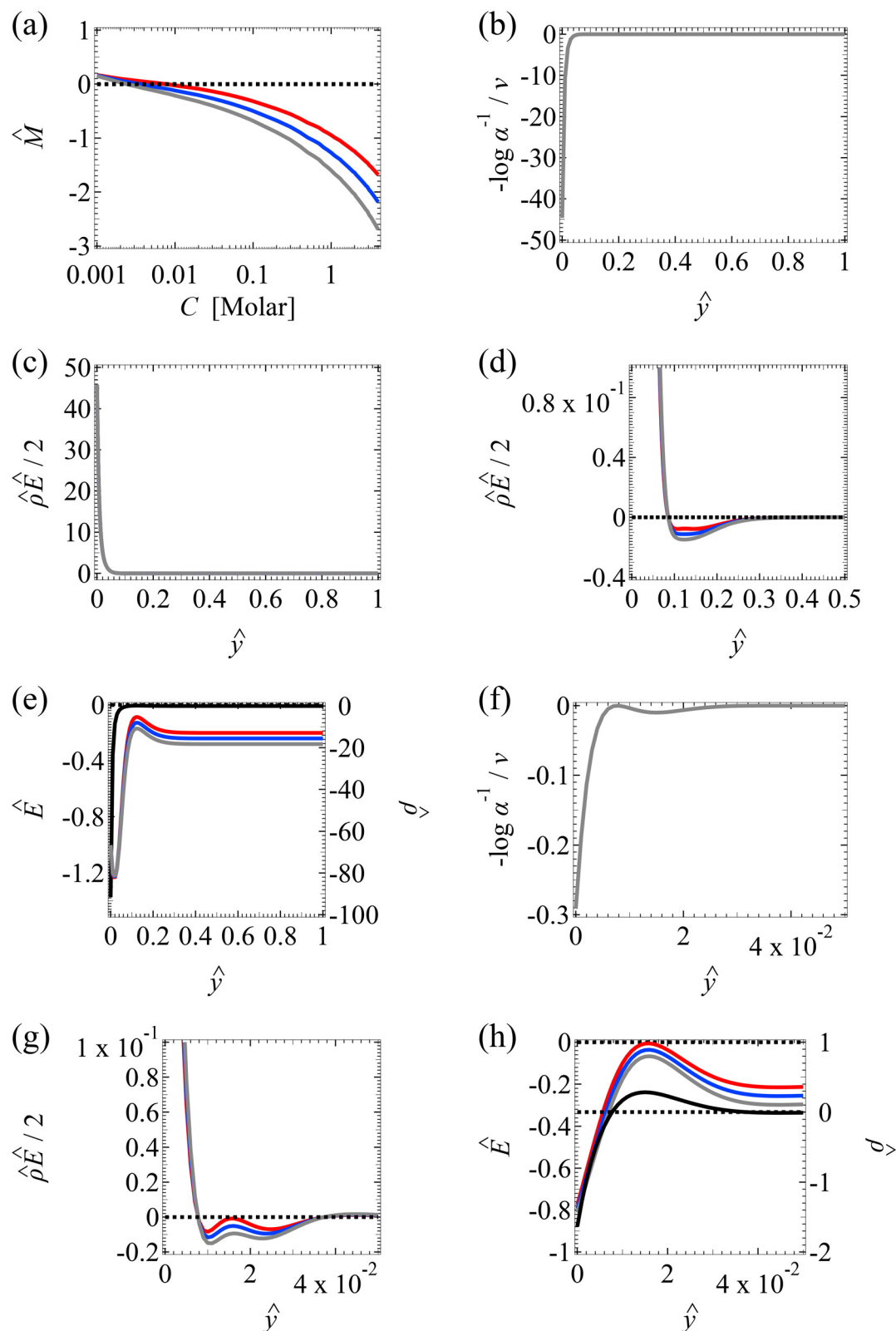


**Fig. 5** Diffusioosmosis of divalent electrolytes accounting for electrostatic correlations ( $\delta_c = \kappa l_c$ ). Figure captions are the same as those in Fig. 4, except that electrostatic correlations are accounted for.

centration of a divalent electrolyte [ $C \approx 0.003$  M in Fig. 5(a)] relative to that of a monovalent electrolyte [ $C \approx 0.4$  M in Fig. 3(a)].

The third new phenomenon caused by electrostatic correlations is that, at  $C \gtrsim 0.003$  M, the mobility continues to increase in magnitude as shown in Fig. 5(a). The physical underpinnings of this phenomenon are the same as the third new phenomenon in section 3.1.2 and are not repeated for brevity.

### 3.2. Diffusioosmotic flow direction diagrams

So far, we have presented results of how the sign and magnitude of the diffusioosmotic mobility (flow) vary with the electrolyte concentration, ion diffusivity difference, and ion valence, at a fixed channel surface charge. In this section, we plot diffusioosmotic flow direction diagrams that show how the sign of the mobility changes with these parameters at varying channel surface charges. The channel height  $H = 100$  nm. Electrostatic correlations are accounted for by incorporating a non-zero  $\delta_c = \kappa\ell_c$ . These diagrams are efficient to identify the range of parameters that generates diffusioosmosis of the desired direction.

We present the diffusioosmotic flow direction diagrams for monovalent electrolytes at  $C = 10^{-3}$  M in Fig. 6(a) and at  $C = 1$  M in Fig. 6(b). The blue lines are obtained by determining the values of  $\beta$  that generate a zero diffusioosmotic mobility (mean diffusioosmotic velocity) at each  $q$  by setting a tolerance of  $M \leq 10^{-4}$ . Thus, the blue lines separate each figure into four domains, each of them corresponding to diffusioosmosis flowing from a region of high to low electrolyte concentration or *vice versa*. We state three key observations associated with electrostatic correlations from these figures as follows.

First, at  $C = 10^{-3}$  M, when  $q$  is positive and as  $\beta$  changes from negative to positive [going from left to right in the top half of Fig. 6(a)], the direction of diffusioosmosis changes from “flowing from a region of low to high electrolyte concentration” (positive mobility) to “flowing from a region of high to low electrolyte concentration” (negative mobility). This observation corresponds to the first and the second observation in section 3.1.1. In contrast, at  $C = 1$  M, when  $q$  is positive and as  $\beta$  changes from negative to positive [going from left to right in the top half of Fig. 6(b)], the direction of diffusioosmosis changes from “flowing from a region of high to low electrolyte concentration” (negative mobility) to “flowing from a region of low to high electrolyte concentration” (positive mobility). This

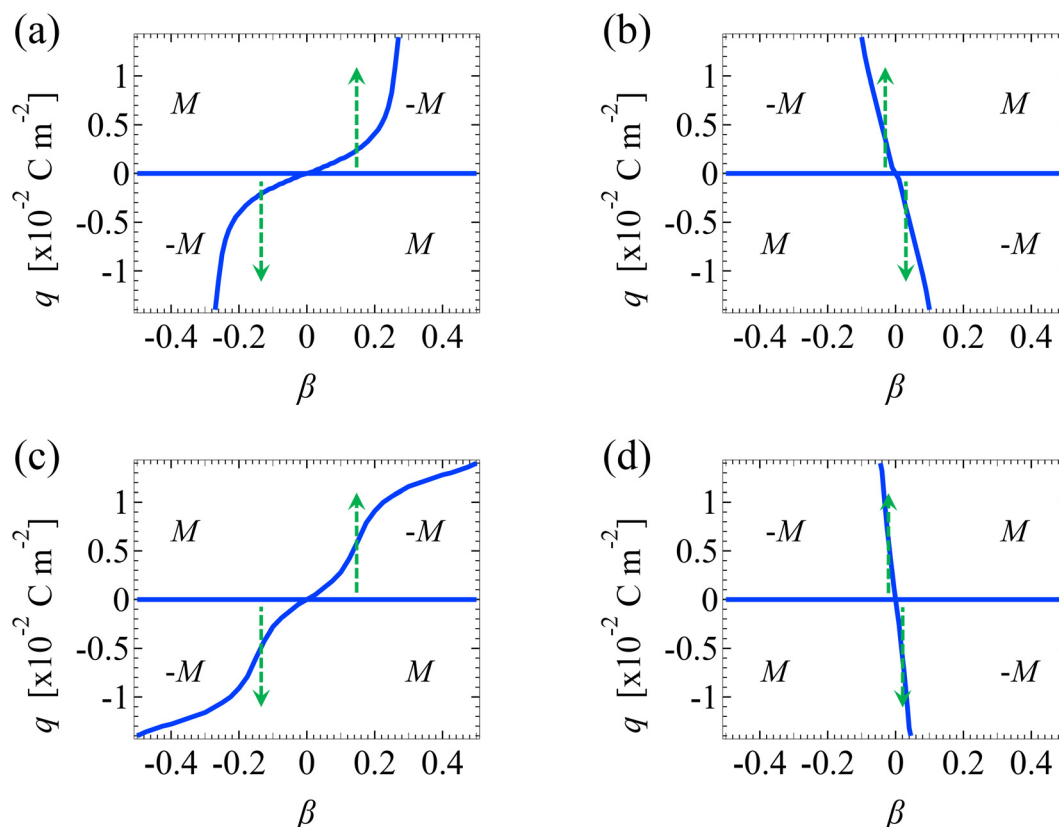


**Fig. 6** Diagrams showing the diffusioosmotic flow direction versus the channel surface charge density  $q$  and ion diffusivity ratio  $\beta$ . The channel height  $H = 100$  nm. (a): Monovalent electrolytes at a bulk electrolyte molar concentration  $C = 10^{-3}$  M. (b): Monovalent electrolytes at  $C = 1$  M. (c): Divalent electrolytes at  $C = 10^{-3}$  M. (d): Divalent electrolytes at  $C = 1$  M. The areas with a positive (negative) mobility  $M$  denote that diffusioosmosis is flowing from a region of low (high) to high (low) electrolyte concentration. Arrows indicate that a diffusioosmotic flow reversal can occur by varying the magnitude of  $q$  without changing its sign.

observation corresponds to the second new phenomenon in section 3.1.2. A diffusioosmotic flow reversal due to electrostatic correlations is demonstrated by comparing the same domain across Fig. 6(a) and (b).

Second, when the magnitude of  $q$  is large (e.g.,  $|q| = 0.014 \text{ C m}^{-2}$ ) and  $\beta$  is small (e.g.,  $|\beta| = 0.02$ ), the direction of diffusioosmosis remains the same across a low [Fig. 6(a)] and a high electrolyte concentration [Fig. 6(b)]. One example of this observation is KCl ( $\beta = -0.02$ ) shown in Fig. 3(a), where the mobility remains positive from low to high electrolyte concentrations.

Third, at a low electrolyte concentration, when  $\beta q > 0$  a diffusioosmotic flow reversal can occur by varying the magnitude of the channel surface charge without changing its sign [e.g., the two arrows in Fig. 6(a)], whereas at a high electrolyte concentration this can only be achieved when  $\beta q < 0$  [e.g., the two arrows in Fig. 6(b)]. This diffusioosmotic flow reversal has been observed in prior work that did not consider electrostatic correlations.<sup>4,8,50,52</sup> That is, this reversal is not due to electrostatic correlations but is a consequence of the competition between the chemiosmotic and electroosmotic components of diffusioosmosis, since it occurs even at a low electrolyte concentration. However, here we remark that electrostatic correlations can radically change the dependence of this reversal on  $\beta q$  between a dilute and a concentrated electrolyte. Before ending, we show the diffusioosmotic flow direction diagrams for divalent electrolytes at  $C = 10^{-3} \text{ M}$  in Fig. 6(c) and at  $C = 1 \text{ M}$  in Fig. 6(d). These figures are qualitatively similar to Fig. 6(a) and (b).

## 4. Conclusions

In this work, we have developed a mathematical model for quantifying the diffusioosmotic flow driven by a binary symmetric electrolyte concentration gradient in a charged parallel-plate channel. The key distinction between this and prior work is the incorporation of ion-ion electrostatic correlations in modeling diffusioosmosis, which is important in concentrated electrolytes but has been ignored in prior theories. The present model also incorporates the steric effect of finite-ion-size, which has been shown to be important in diffusioosmosis of concentrated electrolytes.<sup>14,52</sup> To demonstrate our model, we have computed and analyzed the diffusioosmotic flow mobilities of a list of common monovalent and divalent electrolytes.

In the first part of this article, we have analyzed the variation of the mobilities with respect to the electrolyte concentration. For both monovalent and divalent electrolytes, we have shown that ion-ion electrostatic correlations can lead to a unique reversal of the diffusioosmotic flow. Specifically, electrostatic correlations overscreen the channel surface charge and cause a sign change in the space charge density near the channel surface. This in turn causes a reversal in the electroosmotic driving force of diffusioosmosis, leading to a sign reversal in the diffusioosmotic mobility. Existing theories that ignore electrostatic correlations cannot capture this unique diffusioosmotic flow reversal. Accounting only for the

steric effect of the finite size of ions is not sufficient to capture this flow reversal. This reversal occurs at  $\approx 0.4 \text{ M}$  for a monovalent electrolyte and at a much lower concentration of  $\approx 0.003 \text{ M}$  for a divalent electrolyte in a channel with the same surface charge. These results demonstrate the significant impact of electrostatic correlations on diffusioosmosis, where not just its magnitude but its direction can be altered.

In the second part of this article, we have constructed flow direction diagrams that enable efficient identification of the diffusioosmotic flow direction for a given set of electrolyte concentration, ion diffusivity, ion valence, and channel surface charge. These diagrams predict a separate diffusioosmotic flow reversal that has been identified in prior work.<sup>4,8,50,52</sup> This reversal can occur even at a low electrolyte concentration where electrostatic correlations are negligible. Thus, this reversal is not due to electrostatic correlations but the competition between the chemiosmosis and electroosmosis that constitute diffusioosmosis. This reversal can be achieved by varying the magnitude of the channel surface charge without varying its sign. We show that electrostatic correlations can alter qualitatively how this reversal depends on the product of the channel surface charge and the ion diffusivity difference  $\beta q$  across low to high electrolyte concentrations. Namely, this reversal occurs at a low electrolyte concentration only when  $\beta q > 0$  and at a high electrolyte concentration only when  $\beta q < 0$ .

The present analysis can be extended in several directions. First, a natural extension is to relax the assumption that the equilibrium electric double layer is not perturbed by the diffusioosmotic flow. This can be done by numerically solving the coupled nonlinear systems of the Poisson-Fermi equation, conservation of individual ionic species, and the Stokes equation with an electric body force. However, we note that this extension will likely give quantitative modifications to our present results only and will not alter our conclusions, since the Peclet number is weak [ $Pe \leq O(1)$ ] in diffusioosmosis.<sup>10,50</sup> Second, other effects can be incorporated into the present model, e.g., a concentration-dependent viscosity, diffusivity, and permittivity.<sup>77,79</sup> These effects are, however, prominent only in a solution whose concentration is higher than a few molars. Thus, they will not qualitatively alter the flow reversal predicted from this work, which occurs much below one molar concentration. Third, diffusioosmosis experiments have matured in recent years<sup>9,21</sup> and can measure the diffusioosmotic flow reversal predicted in this work.

## Appendix A: Numerical schemes for solving the electric potential and diffusioosmotic mobility

We describe the numerical schemes for solving the electric potential and diffusioosmotic velocity. Let us start with the governing equation and boundary conditions eqn (4)–(6) for the electric potential. We first discretize the domain  $\hat{y} \in [0, 1]$  into  $m + 1$  grid points  $\hat{y}_0, \hat{y}_1, \dots, \hat{y}_m$ , where  $\hat{y}_i = \hat{y}_0 + i\Delta\hat{y}$  with  $\Delta\hat{y}$

the grid size and  $i = 0, 1, \dots, m$ . The electric potential at the grid point  $\hat{y}_i$  is  $\hat{\phi}_i$ . We approximate the first- and third-order derivatives using a forward finite-difference scheme with a first-order accuracy, and the second- and fourth-order derivatives using a central finite-difference scheme with a second-order accuracy as follows,<sup>80</sup>

$$\frac{d\hat{\phi}_i}{d\hat{y}_i} \approx \frac{-\hat{\phi}_i + \hat{\phi}_{i+1}}{\Delta\hat{y}}, \quad (16)$$

$$\frac{d^2\hat{\phi}_i}{d\hat{y}_i^2} \approx \frac{\hat{\phi}_{i-1} - 2\hat{\phi}_i + \hat{\phi}_{i+1}}{\Delta\hat{y}^2}, \quad (17)$$

$$\frac{d^3\hat{\phi}_i}{d\hat{y}_i^3} \approx \frac{-\hat{\phi}_i + 3\hat{\phi}_{i+1} - 3\hat{\phi}_{i+2} + \hat{\phi}_{i+3}}{\Delta\hat{y}^3}, \quad (18)$$

$$\frac{d^4\hat{\phi}_i}{d\hat{y}_i^4} \approx \frac{\hat{\phi}_{i-2} - 4\hat{\phi}_{i-1} + 6\hat{\phi}_i - 4\hat{\phi}_{i+1} + \hat{\phi}_{i+2}}{\Delta\hat{y}^4}. \quad (19)$$

Upon finite-differencing, eqn (4)–(6) form a system of  $m + 1$  nonlinear equations with  $m + 1$  unknown  $\hat{\phi}_i$ , which are solved by the Newton's method *via* the built-in solver *FindRoot* in Wolfram Mathematica. The diffusioosmotic velocity is solved by the same finite-difference method, except that the highest-order derivative in its governing equation and boundary conditions eqn (13) and (14) is second order. A converged solution of the mean diffusioosmotic velocity, equivalently the diffusioosmotic mobility, is obtained with  $\Delta\hat{y} = 10^{-5}$ . For instance, as shown in Fig. 7, the mobilities at  $C = 10^{-3}$  M obtained with  $\Delta\hat{y} = 10^{-5}$  (solid lines) differ by less than 0.2% from those obtained with  $\Delta\hat{y} = 5 \times 10^{-6}$  (circles).

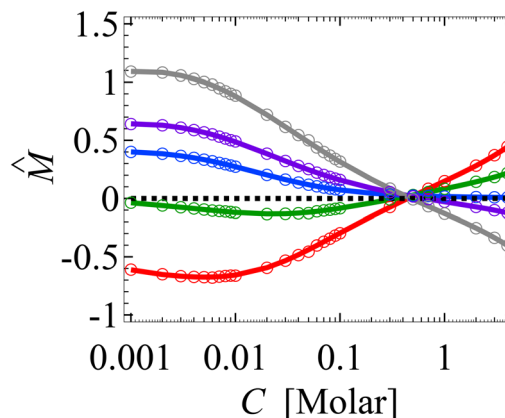


**Fig. 7** Figure captions are the same as those in Fig. 3(a). Solid lines denote results obtained with the grid size  $\Delta\hat{y} = 10^{-5}$  and circles denote results obtained with  $\Delta\hat{y} = 5 \times 10^{-6}$ .

## Appendix B: Model validation by recovering prior work

We validate our model by recovering the results of prior work, which computed the diffusioosmotic mobilities that account for the finite size of ions but ignore electrostatic correlations<sup>52</sup> and those that ignore the finite size of ions and electrostatic correlations.<sup>50</sup> Specifically, as shown by the solid lines in Fig. 8(a), our model recovers the mobilities computed by Hoshyargar *et al.*<sup>52</sup> with  $\nu = 0.05$ ,  $\hat{\zeta} = 6$  and  $Pe = 1$ , in the limit of  $\delta_c = 0$ . As shown by the squares in Fig. 8(a), our model recovers the mobilities computed by Ma and Keh<sup>50</sup> with  $\hat{\zeta} = 6$  and  $Pe = 1$ , in the limit of  $\nu = 0$  and  $\delta_c = 0$ . In short, Fig. 8(a) in this work shows the recovery of Fig. 2(b) in ref. 52, which compares model predictions with and without the finite size of ions in the absence of electrostatic correlations. For an additional reference, we generate a similar set of mobilities with  $\hat{\zeta} = 4$  as shown in Fig. 8(b).

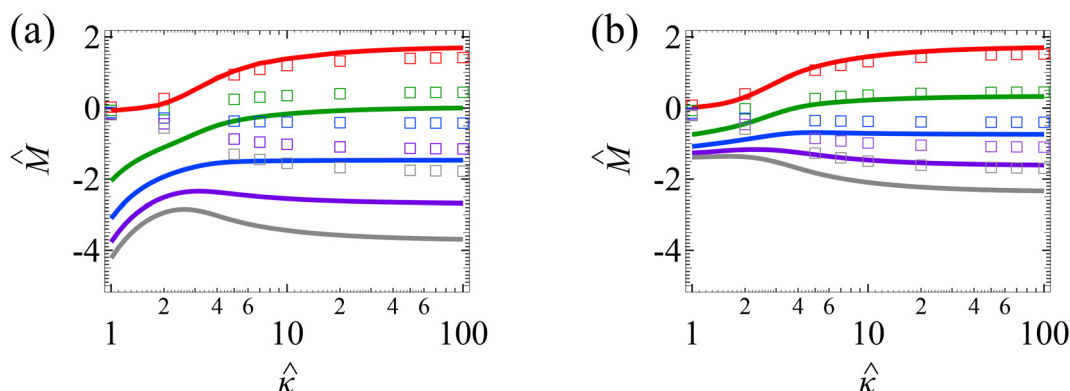


**Fig. 8** For panels (a) and (b), the red solid line and squares denote the ion diffusivity ratio  $\beta = 1$  for the bulk volume fraction of ions  $\nu = 0.05$  and  $\nu = 0$ , respectively; the green solid line and squares denote  $\beta = 0.5$  for  $\nu = 0.05$  and  $\nu = 0$ , respectively; the blue solid line and squares denote  $\beta = 0$  for  $\nu = 0.05$  and  $\nu = 0$ , respectively; the purple solid line and squares denote  $\beta = -0.5$  for  $\nu = 0.05$  and  $\nu = 0$ , respectively; and the grey solid line and squares denote  $\beta = -1$  for  $\nu = 0.05$  and  $\nu = 0$ , respectively. (a): The diffusioosmotic mobility  $\hat{M}$  versus the inverse Debye length  $\hat{\kappa}$  with a channel surface potential  $\hat{\zeta} = 6$ . (b):  $\hat{M}$  versus  $\hat{\kappa}$  with  $\hat{\zeta} = 4$ .



## Conflicts of interest

There are no conflicts of interest to declare.

## Acknowledgements

The authors acknowledge the funding support from the Division of Sponsored Programs, Department of Chemical Engineering, and Herbert Wertheim College of Engineering at University of Florida. This material is based upon work supported by the U.S. Department of Energy, Office of Science, Office of Basic Energy Sciences, Geosciences program under Award Number DE-SC0018676.

## References

- 1 B. V. Derjaguin, G. P. Sidorenkov, E. A. Zubashchenkov and E. V. Kiseleva, *Kolloidnyi Zh.*, 1947, **9**, 335–348.
- 2 J. L. Anderson, *Annu. Rev. Fluid Mech.*, 1989, **21**, 61–99.
- 3 D. Velegol, A. Garg, R. Guha, A. Kar and M. Kumar, *Soft Matter*, 2016, **12**, 4686–4703.
- 4 H. J. Keh, *Curr. Opin. Colloid Interface Sci.*, 2016, **24**, 13–22.
- 5 S. Marbach and L. Bocquet, *Chem. Soc. Rev.*, 2019, **48**, 3102–3144.
- 6 S. Shin, *Phys. Fluids*, 2020, **32**, 101302.
- 7 S. Shim, *Chem. Rev.*, 2022, **122**, 6986–7009.
- 8 D. C. Prieve, J. L. Anderson, J. P. Ebel and M. E. Lowell, *J. Fluid Mech.*, 1984, **148**, 247–269.
- 9 C. Lee, C. Cottin-Bizonne, A. L. Biance, P. Joseph, L. Bocquet and C. Ybert, *Phys. Rev. Lett.*, 2014, **112**, 244501.
- 10 S. Shin, E. Um, B. Sabass, J. T. Ault, M. Rahimi, P. B. Warren and H. A. Stone, *Proc. Natl. Acad. Sci. U. S. A.*, 2016, **113**, 257–261.
- 11 N. Shi, R. Nery-Azevedo, A. I. Abdel-Fattah and T. M. Squires, *Phys. Rev. Lett.*, 2016, **117**, 258001.
- 12 V. Hoshyargar, S. N. Ashrafzadeh and A. Sadeghi, *Phys. Fluids*, 2017, **29**, 012001.
- 13 S. Marbach, H. Yoshida and L. Bocquet, *J. Chem. Phys.*, 2017, **146**, 194701.
- 14 R. F. Stout and A. S. Khair, *Phys. Rev. Fluids*, 2017, **2**, 014201.
- 15 J. T. Ault, S. Shin and H. A. Stone, *J. Fluid Mech.*, 2018, **854**, 420–448.
- 16 F. Raynal, M. Bourgoïn, C. Cottin-Bizonne, C. Ybert and R. Volk, *J. Fluid Mech.*, 2018, **847**, 228–243.
- 17 J. T. Ault, S. Shin and H. A. Stone, *Soft Matter*, 2019, **15**, 1582–1596.
- 18 F. Raynal and R. Volk, *J. Fluid Mech.*, 2019, **876**, 818–829.
- 19 D. Ha, S. Seo, K. Lee and T. Kim, *ACS Nano*, 2019, **13**, 12939–12948.
- 20 H. C. W. Chu, S. Garoff, R. D. Tilton and A. S. Khair, *Soft Matter*, 2020, **16**, 238–246.
- 21 M. K. Rasmussen, J. N. Pedersen and R. Marie, *Nat. Commun.*, 2020, **11**, 2337.
- 22 V. S. Doan, S. Chun, J. Feng and S. Shin, *Nano Lett.*, 2021, **21**, 7625–7630.
- 23 H. C. W. Chu, S. Garoff, R. D. Tilton and A. S. Khair, *J. Fluid Mech.*, 2021, **917**, A52.
- 24 B. M. Alessio, S. Shim, E. Mintah, A. Gupta and H. A. Stone, *Phys. Rev. Fluids*, 2021, **6**, 054201.
- 25 S. Chanda and P. A. Tsai, *Phys. Fluids*, 2021, **33**, 032008.
- 26 H. C. W. Chu, S. Garoff, R. D. Tilton and A. S. Khair, *Soft Matter*, 2022, **18**, 1896–1910.
- 27 B. E. McKenzie, H. C. W. Chu, S. Garoff, R. D. Tilton and A. S. Khair, *J. Fluid Mech.*, 2022, **949**, A17.
- 28 R. E. Migacz and J. T. Ault, *Phys. Rev. Fluids*, 2022, **7**, 034202.
- 29 R. Volk, M. Bourgoïn, C. Brehier and F. Raynal, *J. Fluid Mech.*, 2022, **948**, A42.
- 30 S. Lee, J. Lee and J. T. Ault, *Colloids Surf., A*, 2023, **659**, 130775.
- 31 S. Sambamoorthy and H. C. W. Chu, *Soft Matter*, 2023, **19**, 1131–1143.
- 32 J. Xu, Z. Wang and H. C. W. Chu, *RSC Adv.*, 2023, **13**, 9247–9259.
- 33 I. Ertugrul and O. Ulkir, *RSC Adv.*, 2020, **10**, 33731–33738.
- 34 A. Sharma, M. Bekir, N. Lomadze, S. Jung, A. Pich and S. Santer, *Langmuir*, 2022, **38**, 6343–6351.
- 35 X. Wang and D. Jing, *J. Phys. D: Appl. Phys.*, 2022, **55**, 145401.
- 36 S. K. Mehta and P. K. Mondal, *Electrophoresis*, 2023, **44**, 44–52.
- 37 B. E. Logan and M. Elimelch, *Nature*, 2012, **488**, 313–319.
- 38 A. Siria, P. Poncharal, A. Biance, R. Fulcrand, X. Blase, S. T. Purcell and L. Bocquet, *Nature*, 2013, **494**, 455–458.
- 39 B. D. Kang, H. J. Kim, M. G. Lee and D. Kim, *Energy*, 2015, **86**, 525–538.
- 40 S. Chanda and P. A. Tsai, *Energy*, 2019, **176**, 531–543.
- 41 M. Karimzadeh, M. Khatibi, S. N. Ashrafzadeh and P. K. Mondal, *Phys. Chem. Chem. Phys.*, 2022, **24**, 20303–20317.
- 42 D. Pandey, P. K. Mondal and S. Wongwises, *Soft Matter*, 2023, **19**, 1152–1163.
- 43 A. Kar, T. Chiang, I. O. Rivera, A. Sen and D. Velegol, *ACS Nano*, 2015, **9**, 746–753.
- 44 S. W. Park, J. Lee, H. Yoon and S. Shin, *Energy Fuels*, 2021, **35**, 4885–4892.
- 45 N. Shi and A. Abdel-Fattah, *Phys. Rev. Fluids*, 2021, **6**, 053103.
- 46 H. Tan, A. Banejee, N. Shi, X. Tang, A. Abdel-Fattah and T. M. Squires, *Sci. Adv.*, 2021, **7**, eabh0638.
- 47 H. Zhang, D. Y. Moh, S. Wang and R. Qiao, *Phys. Fluids*, 2022, **34**, 092017.
- 48 H. J. Keh and J. H. Wu, *Langmuir*, 2001, **17**, 4216–4222.
- 49 H. J. Keh and H. C. Ma, *Colloids Surf., A*, 2004, **233**, 87–95.
- 50 H. C. Ma and H. J. Keh, *J. Colloid Interface Sci.*, 2006, **298**, 476–486.
- 51 T. Chiang and D. Velegol, *J. Colloid Interface Sci.*, 2014, **424**, 120–123.

- 52 V. Hoshyargar, S. N. Ashrafizadeh and A. Sadeghi, *Phys. Chem. Chem. Phys.*, 2015, **17**, 29193–29200.
- 53 H. Jing and S. Das, *Phys. Chem. Chem. Phys.*, 2018, **20**, 10204–10212.
- 54 A. Gupta, B. Rallabandi and H. A. Stone, *Phys. Rev. Fluids*, 2019, **4**, 043702.
- 55 A. Y. Grosberg, T. T. Nguyen and B. I. Shklovskii, *Rev. Mod. Phys.*, 2002, **74**, 329–345.
- 56 Y. Levin, *Rep. Prog. Phys.*, 2002, **65**, 1577–1632.
- 57 M. Mezger, H. Schroder, H. Reichert, S. Schramm, J. S. Okasinski, S. Schoder, V. Honkimake, M. Deutsch, B. M. Ocko, J. Ralston, M. Rohwerder, M. Stratmann and H. Dosch, *Science*, 2008, **322**, 424–428.
- 58 G. M. Torrie and J. P. Valleau, *J. Chem. Phys.*, 1980, **73**, 5807–5816.
- 59 E. Gonzales-Tovar, M. Lozada-Cassou and D. Henderson, *J. Chem. Phys.*, 1985, **83**, 361–372.
- 60 R. Kjellander and S. Marcelja, *J. Phys. Chem. A*, 1986, **90**, 1230–1232.
- 61 P. Attard, D. J. Mitchell and B. W. Ninham, *J. Chem. Phys.*, 1988, **89**, 4358–4367.
- 62 J. Ennis, S. Marcelja and R. Kjellander, *Electrochim. Acta*, 1996, **41**, 2115–2124.
- 63 R. R. Netz and H. Orland, *Eur. Phys. J. E: Soft Matter Biol. Phys.*, 2000, **1**, 203–214.
- 64 A. Martin-Molina, M. Quesada-Perez, F. Galisteo-Gonzalez and R. Hidalgo-Alvarez, *J. Chem. Phys.*, 2003, **118**, 4183–4189.
- 65 M. V. Fedorov and A. A. Kornyshev, *J. Phys. Chem. B*, 2008, **112**, 11868–11872.
- 66 M. M. Hatlo and L. Lue, *Europhys. Lett.*, 2010, **89**, 25002.
- 67 D. Gillespie, A. S. Khair, J. P. Bardhan and S. Pennathur, *J. Colloid Interface Sci.*, 2011, **359**, 520–529.
- 68 C. D. Santangelo, *Phys. Rev. E: Stat., Nonlinear, Soft Matter Phys.*, 2006, **73**, 041512.
- 69 M. Bazant, B. D. Storey and A. A. Kornyshev, *Phys. Rev. Lett.*, 2011, **106**, 046102.
- 70 B. D. Storey and M. Z. Bazant, *Phys. Rev. E: Stat., Nonlinear, Soft Matter Phys.*, 2012, **86**, 056303.
- 71 M. He, P. Sun and H. Zhao, *Comput. Math. Appl.*, 2022, **117**, 229–244.
- 72 R. F. Stout and A. S. Khair, *J. Fluid Mech.*, 2014, **752**, R1.
- 73 E. Alidoosti and H. Zhao, *Langmuir*, 2018, **34**, 5592–5599.
- 74 E. Alidoosti and H. Zhao, *Electrophoresis*, 2019, **40**, 2655–2661.
- 75 J. J. Bikerman, *Philos. Mag.*, 1942, **33**, 384–397.
- 76 M. S. Kilic, M. Z. Bazant and A. Ajdari, *Phys. Rev. E: Stat., Nonlinear, Soft Matter Phys.*, 2007, **75**, 021502.
- 77 M. Bazant, M. S. Kilic, B. D. Storey and A. Ajdari, *Adv. Colloid Interface Sci.*, 2009, **152**, 48–88.
- 78 P. Vanysek, *CRC Handbook of Chemistry and Physics*, CRC Press, Boca Raton, 1992.
- 79 Y. Nakayama and D. Andelman, *J. Chem. Phys.*, 2015, **142**, 044706.
- 80 R. J. LeVeque, *Finite difference methods for ordinary and partial differential equations*, Society for Industrial and Applied Mathematics, Philadelphia, 2007.